

## Weakly coupled lithospheric extension in southern Tibet



Xiaobo Tian<sup>a,b,\*</sup>, Yun Chen<sup>a</sup>, Tai-Lin Tseng<sup>c</sup>, Simon L. Klemperer<sup>d</sup>, Hans Thybo<sup>e</sup>, Zhen Liu<sup>a,f</sup>, Tao Xu<sup>a,b</sup>, Xiaofeng Liang<sup>a</sup>, Zhiming Bai<sup>a</sup>, Xi Zhang<sup>a</sup>, Shaokun Si<sup>g</sup>, Changqing Sun<sup>h</sup>, Haiqiang Lan<sup>a</sup>, Erchie Wang<sup>a,b</sup>, Jiwen Teng<sup>a</sup>

<sup>a</sup> State Key Laboratory of Lithospheric Evolution, Institute of Geology and Geophysics, Chinese Academy of Sciences, Beijing 100029, China

<sup>b</sup> CAS Center for Excellence in Tibetan Plateau Earth Sciences, Beijing 100101, China

<sup>c</sup> Department of Geosciences, National Taiwan University, Taipei 10617, Taiwan

<sup>d</sup> Department of Geophysics, Stanford University, Stanford, CA 94305, USA

<sup>e</sup> Department of Geography and Geology, University of Copenhagen, DK-1350 Copenhagen K, Denmark

<sup>f</sup> University of Chinese Academy of Sciences, Beijing 100049, China

<sup>g</sup> Department of Deep-sea Investigation, National Deep Sea Center, State Oceanic Administration, Qingdao 266061, China

<sup>h</sup> Key Laboratory of Crustal Dynamics, Institute of Crustal Dynamics, China Earthquake Administration, Beijing 100085, China

### ARTICLE INFO

#### Article history:

Received 15 April 2015

Received in revised form 11 August 2015

Accepted 19 August 2015

Available online xxxx

Editor: A. Yin

#### Keywords:

Tibetan plateau

E–W extension

N–S trending rift

VDSS

crustal structure

### ABSTRACT

West–east extension is a prominent tectonic feature of southern and central Tibet despite ongoing north–south (N–S) convergence between India and Eurasia. Knowledge of deep structure beneath the N–S trending rifts is key to evaluating models proposed for their origin, including gravitational collapse, oblique convergence along the arcuate plate boundary, and mantle upwelling. We model direct S and Moho-reflected SsPmp phases at teleseismic distances to constrain variations in crustal thickness across the major rifts crossed by a ~900-km long, W–E broadband array in the Lhasa Terrane. Crustal thicknesses are ~70–80 km. However, Moho depth decreases by ~10 km within a horizontal distance of 100 km west of the Yadong–Gulu rift (YGR) and Nyainqentanghla mountains (NQTL). This Moho uplift, taken with deep, extensional focal mechanisms and reduced seismic velocity in the upper mantle, suggests that asthenospheric upwelling has significantly contributed to the pattern of extension across the YGR and NQTL. The ~100-km separation between surface rift and Moho uplift is likely enabled by partial decoupling across a ductile middle crust.

© 2015 The Authors. Published by Elsevier B.V. This is an open access article under the CC BY-NC-ND license (<http://creativecommons.org/licenses/by-nc-nd/4.0/>).

### 1. Introduction

The Tibetan plateau was created by continental collision between India and Eurasia and their ongoing subsequent convergence (e.g., Molnar and Tapponnier, 1978). Observations from focal mechanisms in the upper crust (Copley et al., 2011), Quaternary and active faulting (Armijo et al., 1986), and geodetic deformation (Chen et al., 2004) all indicate that the tectonic regime includes a marked component of normal faulting and eastward extrusion in southern Tibet. The relationship between N–S shortening, uplift, and E–W crustal extension is fundamental to the mechanics of this collisional orogen (England and Houseman, 1989).

The development of N–S trending rifts in southern Tibet began in mid-to-late Miocene as the result of extension or eastward

extrusion (e.g., Armijo et al., 1986). These rifts are regularly distributed, each a few hundred kilometers long and about 200 km apart, extending north from the Himalayas (Yin, 2000) (Fig. 1). The rifts are more prominent south of the Bangong–Nujiang suture (BNS) than further north (Armijo et al., 1986). Their orientations exhibit an axis of symmetry trending ~N10°E along ~87°E (Kapp and Guynn, 2004). Many rifts in southern Tibet cut across the Indus–Yarlung suture (IYS), with the Yadong–Gulu rift (YGR) at ~89°E and North Lunggar rift (NLR) at ~83°E, extending furthest south into the Himalayan range. These two rifts have undergone more total extension than the others (e.g., Chen et al., 2004), and GPS geodesy shows that one-half to two-thirds of the permanent extension between 80°E and 91°E is concentrated across the YGR (Chen et al., 2004).

Based on the absence of significant normal faulting in all areas of the plateau with mean elevation less than 4500 m, Molnar and Tapponnier (1978) proposed that the rifts result from gravitational spreading of upper crust induced by crustal over-thickening or by rapid uplift of the plateau due to delamination (down-welling)

\* Corresponding author at: State Key Laboratory of Lithospheric Evolution, Institute of Geology and Geophysics, Chinese Academy of Sciences, Beijing 100029, China. Tel.: +86 10 8299 8329; fax: +86 10 8299 8001.

E-mail address: [txb@mail.iggcas.ac.cn](mailto:txb@mail.iggcas.ac.cn) (X. Tian).

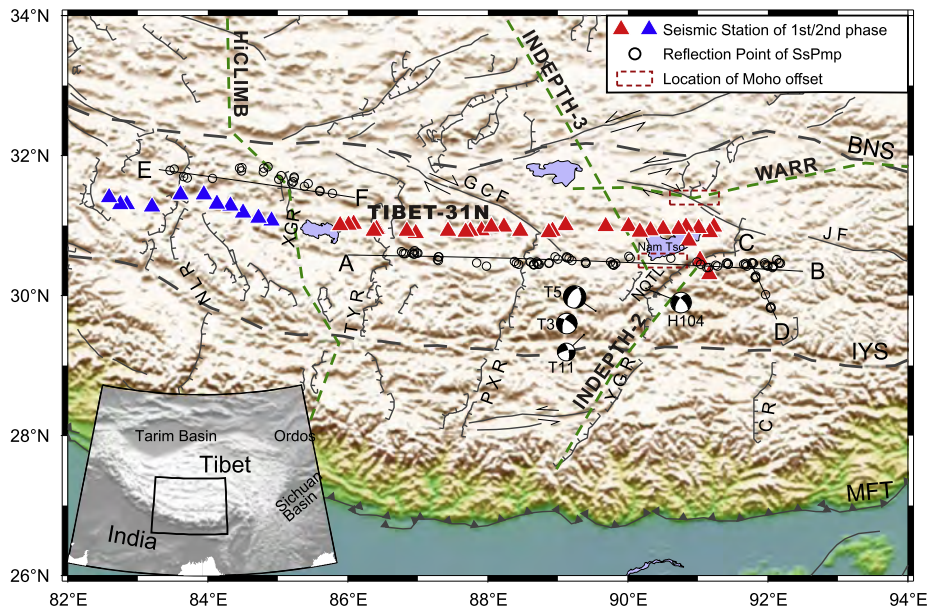


**Fig. 1.** Tectonic and topographic map of southern Tibetan plateau with seismic broadband stations used in this study. Red and blue triangles are the first and second phases of observation, respectively. Open circles mark *SsPmp* reflection points used in this study. Lines labeled AB, CD and EF are segments along which we construct Moho geometry. Green dashed lines represent N–S arrays of HiCLIMB, INDEPTH 2–3 and the E–W profile of wide-angle reflection–refraction (WARR) from Selin Tso to Yaanduo. Purple dashed rectangles mark the locations of Moho offset from Zhang and Klemperer (2005) and this study. Four focal mechanisms are the intermediate-depth earthquakes in southern Tibet (T3, T5 and T11 from Chen and Yang (2004) and Zhu and Helmberger (1996); H104 from Baur (2007), for parameters see Table S4). We show major thrust faults (MFT: Main Frontal Thrust), sutures (BNS: Bangong–Nujiang suture, IYS: Indus–Yarlung suture), strike-slip faults (GCF: Gyaring Co fault, JF: Jiali fault), and south–north trending rifts (CR: Comei rift, YGR: Yadong–Gulu rift, PXR: Pumqu–Xianza rift, TYR: Tangra Yum Co rift, XGR: Xiang–Gangjiang rift, NLR: North Lunggar rift). NQTL: Nyainqentanghla range. Geological structures from Taylor and Yin (2009). An west-dipping normal fault on the western side of the southern NQTL from Kapp et al. (2005) and Kidd et al. (1988).

of the lithospheric mantle (e.g., Molnar et al., 1993). This gravitational collapse model implies that the age of initiation of the rifts should be a proxy for the timing that Tibet achieved its maximum elevation (e.g., Harrison et al., 1992; Molnar et al., 1993). In contrast McCaffrey and Nabelek (1998), noting similarities between the Himalayan arc and subduction along curved oceanic trenches, suggested W–E extension on rifts in the southern Tibet and Himalaya results from oblique convergence along an arcuate margin. In this model, the normal faulting should only occur as far north as the underthrust Indian lithosphere provides a basal shear force (cf. Copley et al., 2011), and the faulting should not continue from the upper crust down into the underthrust plate. McCaffrey and Nabelek (1998) suggested that rifting can occur at any elevation, and that rift initiation is not a proxy for uplift of the plateau. In a third model, Yin (2000) emphasized the broad similarities in the history of volcanism, the age of rift initiation, and the trend and direction of extension of rifts in Tibet, Lake Baikal, and Shanxi. He proposed that all of eastern Asia experienced mantle upwelling beginning at ~40–35 Ma leading to thermal weakening of the lithosphere and eventual rift development at ~8–4 Ma. W–E extension was preceded and accompanied by ultrapotassic N–S trending dikes and adakitic intrusives in southern Tibet implying a magma source in the lithospheric mantle that also triggered melting of an eclogitic lower crust (Hou et al., 2004). Clearly, understanding the structure of the lower crust and uppermost mantle will shed light on the origin of the N–S trending rifts and the E–W extension.

The Lhasa block, bounded by the BNS to the north and IYS to the south (Fig. 1), is an ideal place to investigate the lateral variations of the deep structure beneath and between the rifts. We operated a 900-km-long west–east passive-source linear seismic array (TIBET-31N) along latitude ~31°N in the central Lhasa block, from the Lunggar range to Nam Tso, crossing several major N–S trending rifts (Fig. 1). The seismic array is divided into three segments. Segments AB and CD, composed of 48 and 10 seis-

mographs, respectively, recorded during the first phase of deployment from September 2009 to November 2010 (Chen et al., 2015; Zhang et al., 2013). Segment EF including 13 seismographs was deployed from April 2011 to November 2011. All stations used in this study are also shown in Fig. S1 with station names.

## 2. Data, methods and results

In this study, we use the method of virtual deep seismic sounding (VDSS) developed by Tseng et al. (2009) to investigate the structure of the crust and uppermost of mantle beneath TIBET-31N. Unlike conventional seismic profiling with manmade sources near the surface, VDSS utilizes the conversion of teleseismic *S*- to *P*-wave at the free surface (near the receiver) as a virtual seismic source. The seismic phase *SsPmp* originates as the direct *S*-wave reflects at the free surface and partially converts to a *P*-wave that, in turn, reflects off the Moho before finally arriving at a seismic station. VDSS produces large, clear reflections that are insensitive to details of the Moho transition, thus providing a robust estimate of overall crustal thickness. For the simple case of a uniform crustal layer over a mantle half-space, the differential time between *SsPmp* and *Ss* arrivals is

$$T_{SsPmp-Ss} = 2H(1/V_p^2 - p^2)^{1/2}$$

where *p* is the ray-parameter (horizontal slowness) of the incoming *S*-wave, *H* the crustal thickness, and *V<sub>p</sub>* the *P*-wave speed in the crust.

Among numerous earthquakes that occurred during each phase of the deployment, we choose large to moderate-sized events between epicentral distance of 30° and 50° for which the amplitude of the relevant seismic phases is expected to be large. Some stations have insufficient data due to power problems, including T\_C11, T\_C13 and T\_C14, and are not shown in Figs. 1 and S1. Deep and shallow earthquakes are used in the analysis (Table S1).

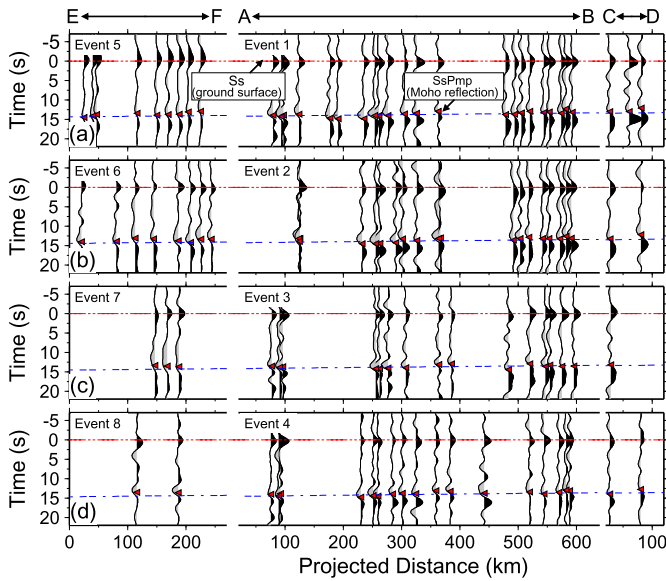


**Fig. 2.** VDSS  $P$ -wave seismic profile using  $SsPmp$  phases from earthquakes listed in Table S1. Seismograms show broadband ground-velocity (vertical-component data deconvolved with the radial component; Gaussian filter applied with  $\alpha = 1.0$ ). Due to total reflection off the Moho,  $SsPmp$  has a phase-shift of  $90 \pm 30^\circ$  compared to the direct  $S$ -wave arrival ( $Ss$ ). Red arrows indicate the Moho  $SsPmp$  reflection phase of Moho based on the waveform fitting in Figs. S3 and S4. All seismograms are plotted at the projected distance of  $SsPmp$  reflection points. The ray parameter changes slightly for each seismogram along the array, and among different earthquakes. For comparison, we plot the predicted  $T_{SsPmp-Ss}$  as blue dashed line on each profile section based on a simple model with a 75-km crust and a  $P$ -wave velocity of 6.3 km/s. Deviations between red arrows and blue lines suggest Moho undulations.

We manually pick the arrival of phase  $S$  on the vertical and radial components. The waveforms were then windowed between  $-10$  s and 35 s relative to  $S$ . A zero-phase Butterworth filter,  $\sim 0.05$ – $0.5$  Hz, is applied to increase the signal-to-noise ratio. In order to enhance both the quality and quantity of results from VDSS, we follow Yu et al. (2013) to remove effects of the earthquake source wavelet and near-source scattering by analyses of particle motion and the deconvolution of the vertical component from the ‘pseudo- $S$ ’ wave. For these events, the amplitude of the  $SsPmp$  phase in the vertical component after deconvolution is sufficiently large to produce a seismic section (Fig. 2). In Fig. 2, seismograms are aligned on their direct  $S$ -wave pulses. Robust signals from the Moho (the  $SsPmp$  phase) are observed from the 8 events.

Note that there is a phase shift of  $90 \pm 30^\circ$  between phases  $Ss$  and  $SsPmp$  because the latter undergoes a total reflection off the Moho. To reliably determine  $T_{SsPmp-Ss}$ , we routinely compare observed and synthetic seismograms calculated using the reflectivity algorithm (Randall, 1989). For a detailed description of the methodology, see Tseng et al. (2009) and Yu et al. (2013). For each seismogram, the corresponding arrival time of  $SsPmp$  varying from  $\sim 12$  s to  $\sim 15$  s is marked by a red triangle (Fig. 2). This type of seismic profile provides a powerful tool to probe the Moho even under greatly thickened crust. Note that  $T_{SsPmp-Ss}$  is as large as 13 to 15 s (corresponding to crustal thicknesses of 70–80 km) and clear changes/offsets of 2.0 s and 2.5 s ( $\geq 10$  km) are found at 150 km and 450 km (projected distance) along segment AB.

To estimate the crustal thickness ( $H$ ) along the VDSS profile in Fig. 2, we model the  $SsPmp$  based on a simple model of average crustal  $V_P$ . We set the average  $V_P$  across the entire profile be about 6.3 km/s, consistent with previous studies in central Tibet (Owens and Zandt, 1997; Zhao et al., 2001). The precise value of  $V_P$  is unimportant for detecting first-order, relative changes in crustal thickness among different stations (Tseng et al., 2009).

For the case at hand, event through  $T_{SsPmp-Ss}$  depends on both  $H$  and  $V_P$ , detailed  $P$ -wave travel-time tomography showed that  $V_P$  varies by less than  $\pm 2\%$  over a distance of 600 km in central Tibet (Hung et al., 2011). Such fluctuations lead to small change of about  $\pm 5$  km in estimated crustal thickness. Therefore, the observed variations in  $T_{SsPmp-Ss}$  in Fig. 2 largely reflect changes in average crustal thickness. Nevertheless, we allow a generous uncertainty of  $\pm 0.1$  km/s in  $V_P$  when calculating the crustal thickness (error-bars in Fig. 3b).

The phase and amplitude of post-critical  $SsPmp$  are sensitive to the  $P$ -wave speed of the uppermost mantle,  $V_{Pn}$ , and thus the trade-off between  $V_{Pn}$  and  $H$  is quite significant. Using the travel times from regional earthquakes along the Hi-CLIMB array, which was conducted along a north–south corridor between  $84^\circ\text{E}$  and  $86^\circ\text{E}$  in Tibet, Griffin et al. (2011) indicate a  $Pn$  speed of about 8.2 km/s beneath Lhasa block and a lower  $Pn$  velocity of 7.8–7.9 km/s beneath the Qiangtang block. Along our profile the  $Pn$  wavespeed (Liang and Song, 2006; Pei et al., 2007) shows only small variations (8.0–8.2 km/s) beneath the Lhasa block (Fig. S2). To minimize uncertainties due to the trade-off between  $V_{Pn}$  and  $H$  in this study, the average  $V_{Pn}$  calculated from Liang and Song (2006) and Pei et al. (2007) is used during the waveform fitting. The comparisons between observed and best-fitting synthetic waveforms are shown in Figs. S3 and S4. The crustal thicknesses estimated by waveform fitting are plotted in Fig. 3b and listed in Table S2, including all 8 events listed in Table S1. To evaluate the effect of the uncertainty of  $V_{Pn}$  on our result, we repeat the waveform fitting with a fixed  $Pn$  speed of 8.0 km/s and 8.1 km/s, respectively. These results (Fig. S5) show that decreasing  $V_{Pn}$  by 0.1 km/s makes the Moho shallower by  $\sim 2$  km.

From east to west our estimated crustal thicknesses  $H_{VDSS}$  along the profile increases from 70 km near D to 75 km near YGR (Fig. 3). From B to A,  $H_{VDSS}$  increases from  $\sim 70$  km beneath B to a maximum value of  $\sim 80$  km beneath YGR. Over distance less than 100 km west of YGR, the Moho shallows by about 10 km, perhaps representing a more abrupt offset that cannot be more tightly constrained due to lack of coverage in this region. From 400 km west to 150 km the Moho again deepens to  $\sim 80$  km, then shallows by  $\sim 10$  km across a distance constrained to be  $\leq 50$  km midway between TYR and PXR. Yet further west, crustal thickness gradually increases from  $\sim 70$  km to  $\sim 75$  km beneath E. No Moho offset is observed beneath XGR and NLR.

### 3. Discussion

#### 3.1. Comparison with previous studies and other methods

Our observed crustal thicknesses are consistent with previous studies. Beneath the Xianggangjiang rift (XGR) the north–south Hi-CLIMB profile has been interpreted to show the same Moho depths as us of 70–75 km from both VDSS and receiver-function (RF) migrations (Tseng et al., 2009). West of NQTL our Moho depth of  $\sim 72$  km agrees with receiver function estimates of  $\sim 68$  km (Kind et al., 2002) within the uncertainty of the methods. We also find good agreement between our VDSS results along the AB segment and RF images created from data recorded at the same stations, and also with a collinear wide-angle reflection–refraction (WARR) profile (Fig. S6). Using stations of segment CD, Zhang et al. (2013) used RF to show crustal thickening from 70 to 75 km westward across YGR from stations D03 to D07, similar to our VDSS observations of westward crustal thickening along both the CD segment and from 480 km to 600 km of AB (Fig. 3b). Finally,  $\sim 50$  km north of the easternmost AB seismographs, Zhang and Klemperer (2005) interpreted a 500-km-long W–E WARR profile to show a west–east increase of  $\sim 10$  km in crustal thickness just west of the northernmost Yadong–Gulu rift (Fig. 1). If this west–east increase in depth

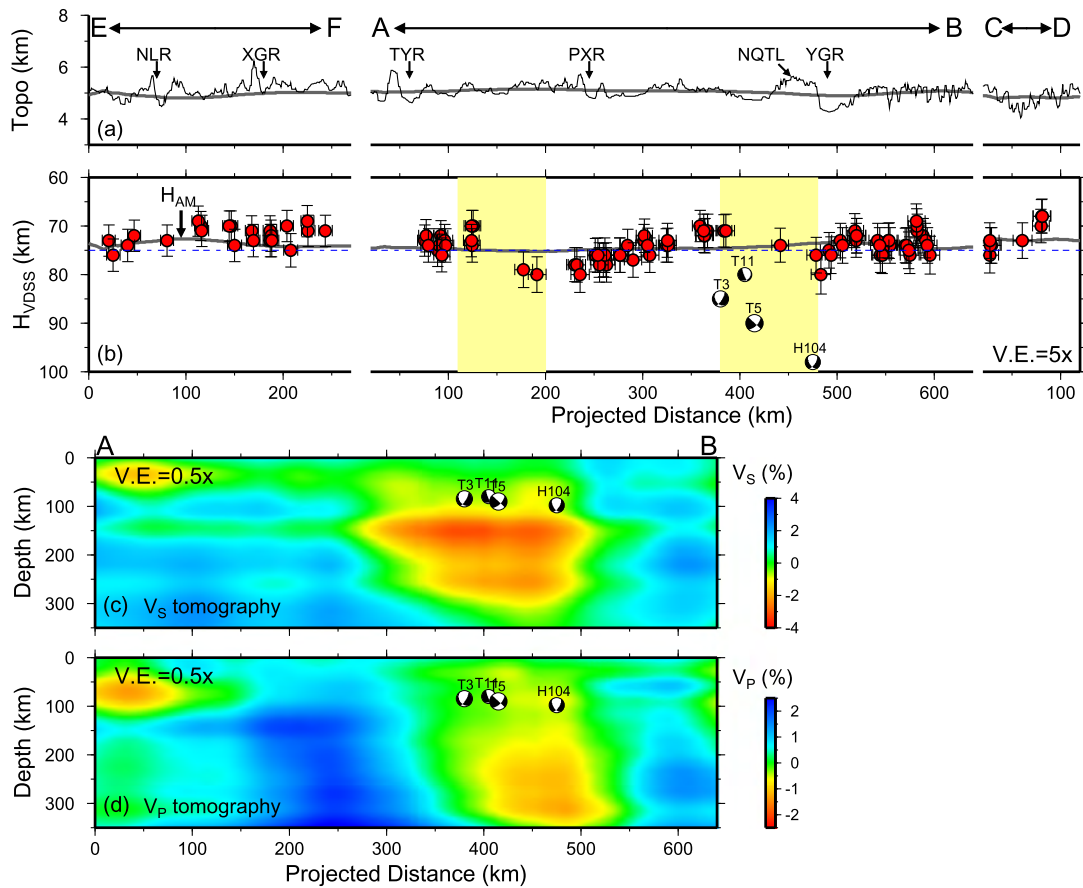


**Fig. 3.** East–west trending profile across rifts in southern Tibet, showing topography and estimated crustal thickness. (a) Elevation along segments in Fig. 1 and mean elevation (thick grey curve) smoothed across 200 km (the approximate separation between each virtual seismic source and station). (b) Estimated crustal thickness ( $H_{VDSS}$ , red dots) based on waveform fitting (Figs. S3 and S4). Vertical and horizontal bars indicate estimated errors in crustal thickness and projected distance from uncertainties in the average crustal  $P$ -wavespeed. The blue dashed line and the grey curve show a reference depth (75-km) and prediction of Airy isostatic Moho ( $H_{AM}$ ), respectively. Focal mechanisms in Fig. 1 are projected onto the profile. Yellow bands mark the location of Moho offset. (c) and (d) are  $V_S$  and  $V_P$  tomographic results (Liang et al., submitted for publication) along AB, with focal mechanisms projected as in (b).

is the same structural feature as the Moho offset immediately west of YGR in Fig. 3b, the Moho step would trend  $\sim$ NNE, essentially parallel with the rift system.

Although there are small discrepancies between the RF and VDSS results (Fig. S6b), these may simply be due to the separation by  $\sim$ 50 km of the RF Moho-conversion point and the VDSS Moho-reflection point, or by lateral variations of crustal  $V_P/V_S$  ratio to which the different methods show different sensitivity. We also note that synthetic waveform modeling (Fig. S7) shows that with a gradational or layered Moho transition the Ps phase used in RF imaging is typically low-amplitude and sensitive to the details of the Moho transition. In contrast, VDSS produces clear, high-amplitude  $SsPmp$  reflections that are less sensitive to fine details, thus providing a more robust estimate of overall crustal thickness.

### 3.2. Deviation from airy isostasy

For illustrative purposes, the average density of crust is taken to be  $2800 \text{ kg/m}^3$ , neglecting lateral variation. The density increase across the Moho is assumed to be  $450 \text{ kg/m}^3$  with a reference crustal thickness of 38 km at sea-level (Jimenez-Munt et al., 2008; Tseng et al., 2009). We use topography smoothed over 200 km (Fig. 3a) and assume pure Airy isostasy to predict values of crustal thickness or depth to the “gravity Moho” ( $H_{AM}$ ) (Fig. 3b). We then use our observed Moho depths ( $H_{VDSS}$ ) to derive a residual crustal thickness,  $H_{VDSS} - H_{AM}$ . Because  $H_{AM}$  only varies by  $\pm 1$  km, we see significant residuals. We find negative residuals of

$\sim 5$  km (isostatic Moho deeper than VDSS Moho) west of NQTL, but  $\sim 5$  km positive residuals (less thinning than expected from the isostatic assumption) beneath both the YGR and the PXR. Unlike typical continental rifts where crust is coaxially and symmetrically stretched and thinned (e.g. North Sea rift: Klempner and White, 1989), we observe most crustal thinning between the rifts rather than beneath the rifts. The separation between the surface rift and the deep structure is consistent with the crustal thinning being associated with the mantle earthquakes (Baur, 2007; Chen and Yang, 2004; Zhu and Helmberger, 1996) and reduced seismic wavespeeds (Liang et al., submitted for publication) that lie west of NQTL (Figs. 3b, 3c and 3d).

### 3.3. Extension of crust and upper mantle beneath NQTL and YGR

Published focal mechanisms (Baur, 2007; Chen et al., 1981; Molnar and Chen, 1983; Zhu and Helmberger, 1996) and the Global CMT Catalogue (Dziewonski et al., 1981; Ekstrom et al., 2012) (Figs. 3 and S8) show W–E extension in both the upper crust and in the mantle lithosphere. In Fig. 4a we project earthquake locations (Fig. S8, Tables S3, S4 and S5) along strike of the YGR onto segment AB. Geological mapping (Armijo et al., 1986; Kidd et al., 1988) supports the inferences we draw from the focal mechanisms (Fig. 4) that along our profile the YGR is a graben, dominated by slip on the east-dipping normal faults on its west side and that a smaller half-graben exists west of the southern part of NQTL.

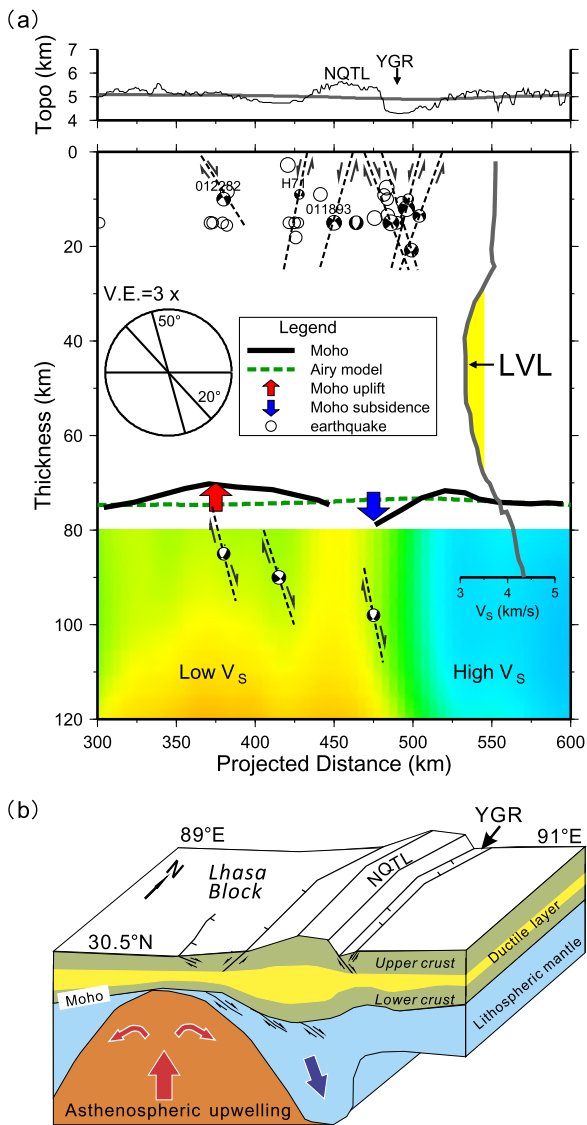


**Fig. 4.** (a) Crustal and uppermost-mantle structure beneath NQTL and YGR along segment AB in distance range from 300 to 600 km. Topography (thin black curve) and smoothed topography (thick grey curve) are shown at top. Thick solid curves are our VDSS Moho (Fig. 3); dashed green line is Moho predicted by Airy isostasy. Red and blue arrows indicate Moho displacement with respect to the Airy model.  $V_s$  tomography (Liang et al., submitted for publication) is shown in the depth range from 80 to 120 km, using the color scale of Fig. 3d. Earthquakes in Fig. S8 are projected to the profile ~NE along strike of the YGR. Fault orientations (thin black dashed lines) based on focal mechanisms (Chen and Yang, 2004; Zhu and Helmberger, 1996; Baur, 2007; Dziewonski et al., 1981; Ekstrom et al., 2012). The low  $V_s$  velocity layer (LVL, in yellow) revealed by dispersion and amplitude analysis of Rayleigh waves (Cotte et al., 1999) is plotted as an inset between depth 0 and 90 km. (b) Cartoon illustrating weakly coupled relation between the surface and deep structure. Horizontal shear of the ductile middle crust permits the lateral separation between the surface rift and the Moho uplift.

The discrepancy between our VDSS Moho depth and the Moho depth predicted by the Airy model (Fig. 4a) indicates Moho uplift or depression from its equilibrium depth. We speculate that our observed variations in crustal thickness are due to east-dipping normal faults in the lithospheric mantle as indicated by the earthquakes. The observation within the YGR (north of 30°N) of elevated geothermal  $^3\text{He}/^4\text{He}$  ratios characteristic of a mantle source (Hoke et al., 2000) requires a fluid pathway from the mantle into the crust, perhaps provided by east-dipping faults associated with our observed Moho offset. Further,  $P$ - and  $S$ -wave tomography in-

dicates low wavespeeds in the upper mantle, consistent with active rifting driven by mantle upwelling (Fig. 4a; Liang et al., submitted for publication).

The middle crust of the Lhasa block is characterized by low seismic velocity (e.g., Cotte et al., 1999) and high electrical conductivity (high fluid content) (e.g., Wei et al., 2001), leading to the belief that the middle crust is weak and decouples upper-crustal from lower-lithospheric deformation (Klemperer, 2006). In particular, lateral flow within the middle crust has been suggested to accommodate the extension of Tibet at depth (Cogan et al., 1998). Based on the spatial correlation among the instantaneous strain-rate field obtained from GPS data, active fault traces and fast polarization direction of shear-wave splitting in the upper mantle under Tibet, Yin and Taylor (2011) however suggest that the upper crust and the mantle lithosphere are deformed in a coherent fashion. If upper crust and upper mantle are weakly coupled, there is no need for extension to be coaxial through the lithosphere, which may instead be localized by active processes in the upper mantle and pre-existing weaknesses in the upper crust. Low-viscosity middle crust can also absorb long-wavelength deformation of the mantle lithosphere induced by mantle upwelling, allowing even weak far-field tectonic stresses to trigger anisotropic strain localizations and create short-wavelength asymmetric deformation (Burov and Gerya, 2014).

A 15-km-thick high seismic velocity layer above the Moho in the southern Lhasa block, to ~31°N, is imaged by RF studies (Kind et al., 2002; Nabelek et al., 2009) and explained as eclogitized Indian lower crust underthrust beneath Tibet (Nabelek et al., 2009). A wave of rapid extension on north-trending rifts has been attributed to thickening of the lower crust in southern Tibet as the Indian plate is underthrust (Styron et al., 2015). It is uncertain whether the ~31°N northern limit of underthrust Indian crust and the “mantle suture” (southern limit of Tibetan/Asian mantle at the Moho) are at the same latitude (Nabelek et al., 2009) or if Indian mantle delaminates and subducts further south (Shi et al., 2015). Near the displaced Moho west of YGR, the velocity immediately beneath the Moho exhibit rapid lateral change (Fig. 4). Our finding correlates with either the mantle suture being south of our  $SsPmp$  reflection points at c. 30.2°N, or simply a tear in the underthrusting Indian lithosphere (Chen et al., 2015; Liang et al., submitted for publication).

The cartoon of Fig. 4b summarizes our interpretation of the dynamics of continuing extension across the NQTL and YGR. Our model, although with a weak layer in the middle crust, is different from the extreme version of the channel-flow model which requires no extension at the base of the crust. Instead, lithospheric extension suggests that the upper crust and the mantle lithosphere are deformed in weakly coupled fashion. It is worth noting that our seismic data cannot resolve whether the same tectonic setting triggered initiation of extension (at  $\geq 8$  Ma), or even the latest pulse of magmatism in the NQTL (24–8 Ma) (Kapp et al., 2005).

Unlike YGR and NQTL where the Moho offset is also accompanied with low-velocity anomaly in mantle lithosphere, the main other offset west of PXR (at the projected distance of 120–250 km in Fig. 3) is underlain by a normal mantle lithosphere without sub-crustal earthquakes. The GPS study shows very little extension near PXR in compared with prominent extension in YGR (Chen et al., 2004). Therefore, we speculate that the formation of the rift system on the surface of the plateau may be similar, while the deeper structure could be further influenced by the local asthenospheric flow. Recent thermalchronological data in Lunggar rift suggest that the acceleration of extension from late Miocene to Pliocene in southern Tibet can be better explained by the underthrusting of India rather than gravitational collapse (Styron et al., 2015). Whether and how mantle flow in the asthenosphere is involved

during the development of rift system requires comparisons of geochemical and geophysical constraints under different rifts.

#### 4. Conclusions

The N–S trending rifts are the most prominent active deformation features in the southern Tibetan plateau, demonstrating lateral extension during continental convergence and plateau uplift. Lithospheric structure is a critical constraint on our understanding of the rifts. Teleseismic *SsPmp* phases recorded on our W–E trending broadband seismic array show rapid changes in Moho depth immediately west of the Nyainqentanghla range and the Yadong–Gulu rift (YGR). Combining our results with focal-mechanism and the seismic-tomography studies, we attribute continued extension of the YGR north of the Yarlung–Zangbo suture zone to lithospheric deformation in response to asthenospheric upwelling and far-field W–E extensional stresses. Lateral offset between the YGR and the Moho offset is permitted by changes in mechanical strength across the ductile middle crust.

#### Acknowledgements

We would like to express the deepest memory to the former group leader Prof. Zhongjie Zhang, who led his group to carry out field seismic investigations of “TIBET-31N array” and others research projects in Tibet. Most figures are plotted using the Generic Mapping Tools (Wessel and Smith, 1998). This research is supported by the Strategic Priority Research Program (B) of the Chinese Academy of Sciences (Grant XDB03010700), Sinoprobe-02-02, and the National Natural Science Foundation of China (Grant 41274066). Seismic instruments were provided by the Seismological Experiment Laboratory, IGGCAS.

#### Appendix A. Supplementary material

Supplementary material related to this article can be found online at <http://dx.doi.org/10.1016/j.epsl.2015.08.025>.

#### References

- Armijo, R., Tapponnier, P., Mercier, J.L., Han, T.L., 1986. Quaternary extension in Southern Tibet – field observations and tectonic implications. *J. Geophys. Res., Solid Earth* 91, 13803–13872.
- Bai, Z.M., Zhang, Z., Lu, Q., Klemperer, S.L., Mooney, W., Xu, T., Teng, J., Chen, Y., Tian, X., Sun, R., Yuan, Q., Li, Y., Zhang, X., Zhao, B., submitted for publication. Crustal structure of the central Lhasa block, Tibet from a west–east seismic refraction/wide-angle reflection profile. *Geophys. J. Int.*
- Baur, J.R., 2007. *Seismotectonics of the Himalayas and the Tibetan Plateau: Moment Tensor Analysis of Regional Seismograms*. Oregon State University, Corvallis, OR, p. 275.
- Burov, E., Gerya, T., 2014. Asymmetric three-dimensional topography over mantle plumes. *Nature* 513, 85–89.
- Chen, Q.Z., Freymueller, J.T., Yang, Z.Q., Xu, C.J., Jiang, W.P., Wang, Q., Liu, J.N., 2004. Spatially variable extension in southern Tibet based on GPS measurements. *J. Geophys. Res.* 109, B09401. <http://dx.doi.org/10.1029/2002jb002350>.
- Chen, W.P., Nabelek, J.L., Fitch, T.J., Molnar, P., 1981. An intermediate depth earthquake beneath Tibet – source characteristics of the event of September 14, 1976. *J. Geophys. Res.* 86, 2863–2876.
- Chen, W.P., Yang, Z.H., 2004. Earthquakes beneath the Himalayas and Tibet: evidence for strong lithospheric mantle. *Science* 304, 1949–1952.
- Chen, Y., Li, W., Yuan, X., Badal, J., Teng, J., 2015. Tearing of the Indian lithospheric slab beneath southern Tibet revealed by SKS-wave measurements. *Earth Planet. Sci. Lett.* 413, 13–24.
- Cogan, M.J., Nelson, K.D., Kidd, W.S.F., Wu, C.D., Team, P.I., 1998. Shallow structure of the Yadong–Gulu rift, southern Tibet, from refraction analysis of project INDEPTH common midpoint data. *Tectonics* 17, 46–61.
- Copley, A., Avouac, J.P., Wernicke, B.P., 2011. Evidence for mechanical coupling and strong Indian lower crust beneath southern Tibet. *Nature* 472, 79–81.
- Cotte, N., Pedersen, H., Campillo, M., Mars, J., Ni, J.F., Kind, R., Sandvol, E., Zhao, W., 1999. Determination of the crustal structure in southern Tibet by dispersion and amplitude analysis of Rayleigh waves. *Geophys. J. Int.* 138, 809–819.
- Dziewonski, A.M., Chou, T.A., Woodhouse, J.H., 1981. Determination of earthquake source parameters from waveform data for studies of global and regional seismicity. *J. Geophys. Res.* 86, 2825–2852.
- Ekstrom, G., Nettles, M., Dziewonski, A.M., 2012. The global CMT project 2004–2010: centroid-moment tensors for 13 017 earthquakes. *Phys. Earth Planet. Inter.* 200, 1–9.
- Engdahl, E.R., van der Hilst, R., Buland, R., 1998. Global teleseismic earthquake relocation with improved travel times and procedures for depth determination. *Bull. Seismol. Soc. Am.* 88, 722–743.
- England, P., Houseman, G., 1989. Extension during continental convergence, with application to the Tibetan plateau. *J. Geophys. Res., Solid Earth* 94, 17561–17579.
- Griffin, J.D., Nowack, R.L., Chen, W.P., Tseng, T.L., 2011. Velocity structure of the Tibetan lithosphere: constraints from P-wave travel times of regional earthquakes. *Bull. Seismol. Soc. Am.* 101, 1938–1947.
- Harrison, T.M., Copeland, P., Kidd, W.S.F., Yin, A., 1992. Raising Tibet. *Science* 255, 1663–1670.
- Hoke, L., Lamb, S., Hilton, D.R., Poreda, R.J., 2000. Southern limit of mantle-derived geothermal helium emissions in Tibet: implications for lithospheric structure. *Earth Planet. Sci. Lett.* 180, 297–308.
- Hou, Z.Q., Gao, Y.F., Qu, X.M., Rui, Z.Y., Mo, X.X., 2004. Origin of adakitic intrusives generated during mid-Miocene east–west extension in southern Tibet. *Earth Planet. Sci. Lett.* 220, 139–155.
- Hung, S.H., Chen, W.P., Chiao, L.Y., 2011. A data-adaptive, multiscale approach of finite-frequency, traveltimes tomography with special reference to P and S wave data from central Tibet. *J. Geophys. Res., Solid Earth* 116, B06307. <http://dx.doi.org/10.1029/2010jb008190>.
- Jimenez-Munt, I., Fernandez, M., Verges, J., Platt, J.P., 2008. Lithosphere structure underneath the Tibetan Plateau inferred from elevation, gravity and geoid anomalies. *Earth Planet. Sci. Lett.* 267, 276–289.
- Kapp, J.L.D., Harrison, T.M., Kapp, P., Grove, M., Lovera, O.M., Lin, D., 2005. Nyainqentanghla Shan: a window into the tectonic, thermal, and geochemical evolution of the Lhasa block, southern Tibet. *J. Geophys. Res., Solid Earth* 110, B08413. <http://dx.doi.org/10.1029/2004jb003330>.
- Kapp, P., Guynn, J.H., 2004. Indian punch rifts Tibet. *Geology* 32, 993–996.
- Kidd, W.S.F., Pan, Y.S., Chang, C.F., Coward, M.P., Dewey, J.F., Gansser, A., Molnar, P., Shackleton, R.M., Sun, Y.Y., 1988. Geological mapping of the 1985 Chinese–British Tibetan (Xizang–Qinghai) Plateau Geotraverse Route. *Philos. Trans. R. Soc. Lond. A* 327, 287–305.
- Kind, R., Yuan, X., Saul, J., Nelson, D., Sobolev, S.V., Mechie, J., Zhao, W., Kosarev, G., Ni, J., Achauer, U., Jiang, M., 2002. Seismic images of crust and upper mantle beneath Tibet: evidence for Eurasian plate subduction. *Science* 298, 1219–1221.
- Klemperer, S.L., 2006. Crustal flow in Tibet: geophysical evidence for the physical state of Tibetan lithosphere, and inferred patterns of active flow. *Geol. Soc. (Lond.) Spec. Publ.* 268, 39–70.
- Klemperer, S.L., White, N., 1989. Coaxial stretching or lithospheric simple shear in the North Sea? Evidence from deep seismic profiling and subsidence. *AAPG Mem.* 46, 511–522.
- Liang, C.T., Song, X.D., 2006. A low velocity belt beneath northern and eastern Tibetan Plateau from Pn tomography. *Geophys. Res. Lett.* 33, L22306. <http://dx.doi.org/10.1029/2006gl027926>.
- Liang, X.F., Chen, Y., Tian, X., Wang, M., Xu, T., Sun, C.Q., Si, S.K., Lan, H.Q., Teng, J., submitted for publication. Frontier of the underthrusting Indian lithosphere beneath the central Tibet from finite frequency tomography. *Gondwana Res.*
- McCaffrey, R., Nabelek, J., 1998. Role of oblique convergence in the active deformation of the Himalayas and southern Tibet plateau. *Geology* 26, 691–694.
- Molnar, P., Chen, W.P., 1983. Focal depths and fault plane solutions of earthquakes under the Tibetan Plateau. *J. Geophys. Res.* 88, 1180–1196.
- Molnar, P., England, P., Martinod, J., 1993. Mantle dynamics, uplift of the Tibetan Plateau, and the Indian Monsoon. *Rev. Geophys.* 31, 357–396.
- Molnar, P., Tapponnier, P., 1978. Active tectonics of Tibet. *J. Geophys. Res.* 83, 5361–5375.
- Nabelek, J., Hetenyi, G., Vergne, J., Sapkota, S., Kafle, B., Jiang, M., Su, H.P., Chen, J., Huang, B.S., Team, H.-C., 2009. Underplating in the Himalaya–Tibet collision zone revealed by the Hi-CLIMB experiment. *Science* 325, 1371–1374.
- Owens, T.J., Zandt, G., 1997. Implications of crustal property variations for models of Tibetan plateau evolution. *Nature* 387, 37–43.
- Pei, S.P., Zhao, J.M., Sun, Y.S., Xu, Z.H., Wang, S.Y., Liu, H.B., Rowe, C.A., Toksoz, M.N., Gao, X., 2007. Upper mantle seismic velocities and anisotropy in China determined through Pn and Sn tomography. *J. Geophys. Res., Solid Earth* 112, B05312. <http://dx.doi.org/10.1029/2006jb004409>.
- Randall, G.E., 1989. Efficient calculation of differential seismograms for lithospheric receiver functions. *Geophys. J. Int.* 99, 469–481.
- Shi, D., Wu, Z., Klemperer, S.L., Zhao, W., Xue, G., Su, H., 2015. Receiver function imaging of crustal suture, steep subduction, and mantle wedge in the eastern India–Tibet continental collision zone. *Earth Planet. Sci. Lett.* 414, 6–15.
- Styron, R., Taylor, M., Sundell, K., 2015. Accelerated extension of Tibet linked to the northward underthrusting of Indian crust. *Nat. Geosci.* 8, 131–134.
- Taylor, M., Yin, A., 2009. Active structures of the Himalayan–Tibetan orogen and their relationships to earthquake distribution, contemporary strain field, and Cenozoic volcanism. *Geosphere* 5, 199–214.

- Tseng, T.L., Chen, W.P., Nowack, R.L., 2009. Northward thinning of Tibetan crust revealed by virtual seismic profiles. *Geophys. Res. Lett.* 36, L24304. <http://dx.doi.org/10.1029/2009gl040457>.
- Wei, W.B., Unsworth, M., Jones, A., Booker, J., Tan, H.D., Nelson, D., Chen, L.S., Li, S.H., Solon, K., Bedrosian, P., Jin, S., Deng, M., Ledo, J., Ray, D., Roberts, B., 2001. Detection of widespread fluids in the Tibetan crust by magnetotelluric studies. *Science* 292, 716–718.
- Wessel, P., Smith, W.H.F., 1998. New, improved version of the generic mapping tools released. *Eos Trans. AGU* 79, 579.
- Yin, A., 2000. Mode of Cenozoic east–west extension in Tibet suggesting a common origin of rifts in Asia during the Indo–Asian collision. *J. Geophys. Res., Solid Earth* 105, 21745–21759.
- Yin, A., Taylor, M.H., 2011. Mechanics of V-shaped conjugate strike-slip faults and the corresponding continuum mode of continental deformation. *Geol. Soc. Am. Bull.* 123, 1798–1821.
- Yu, C.Q., Chen, W.P., van der Hilst, R.D., 2013. Removing source-side scattering for virtual deep seismic sounding (VDSS). *Geophys. J. Int.* 195, 1932–1941.
- Zhang, Z.J., Chen, Y., Yuan, X.H., Tian, X.B., Klempere, S.L., Xu, T., Bai, Z.M., Zhang, H.S., Wu, J., Teng, J.W., 2013. Normal faulting from simple shear rifting in South Tibet, using evidence from passive seismic profiling across the Yadong–Gulu Rift. *Tectonophysics* 606, 178–186.
- Zhang, Z.J., Klempere, S.L., 2005. West–east variation in crustal thickness in northern Lhasa block, central Tibet, from deep seismic sounding data. *J. Geophys. Res., Solid Earth* 110, B09403. <http://dx.doi.org/10.1029/2004jb003139>.
- Zhao, W., Mechie, J., Brown, L.D., Guo, J., Haines, S., Hearn, T., Klempere, S.L., Ma, Y.S., Meissner, R., Nelson, K.D., Ni, J.F., Pananont, P., Rapine, R., Ross, A., Saul, J., 2001. Crustal structure of central Tibet as derived from project INDEPTH wide-angle seismic data. *Geophys. J. Int.* 145, 486–498.
- Zhu, L.P., Helmberger, D.V., 1996. Intermediate depth earthquakes beneath the India–Tibet collision zone. *Geophys. Res. Lett.* 23, 435–438.

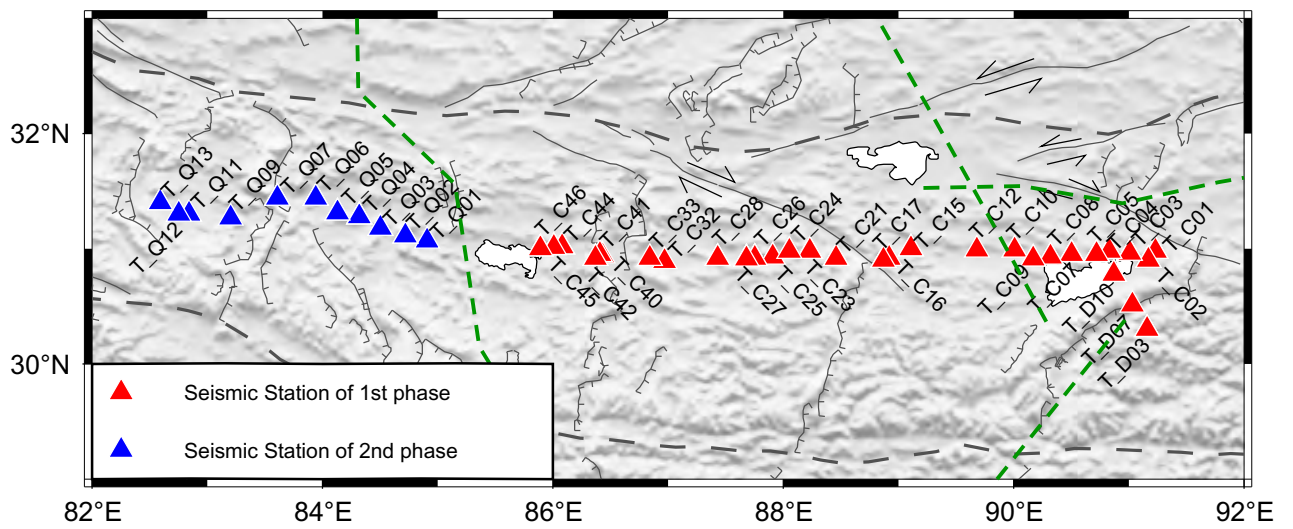


Figure S1

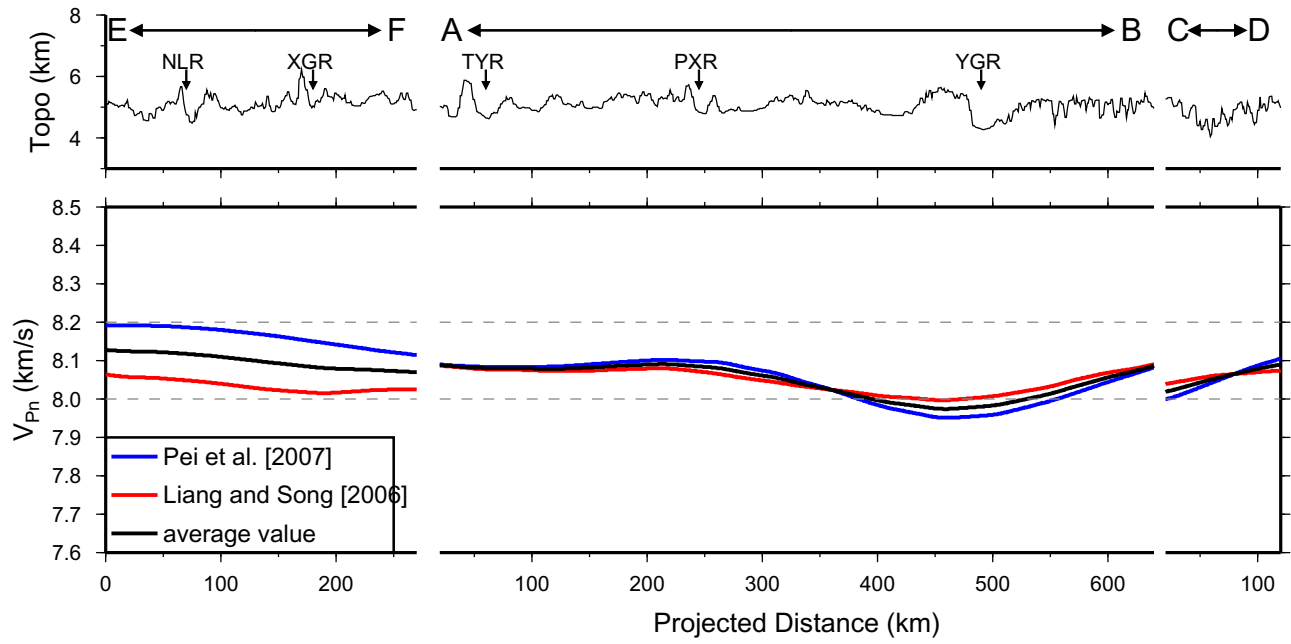


Figure S2

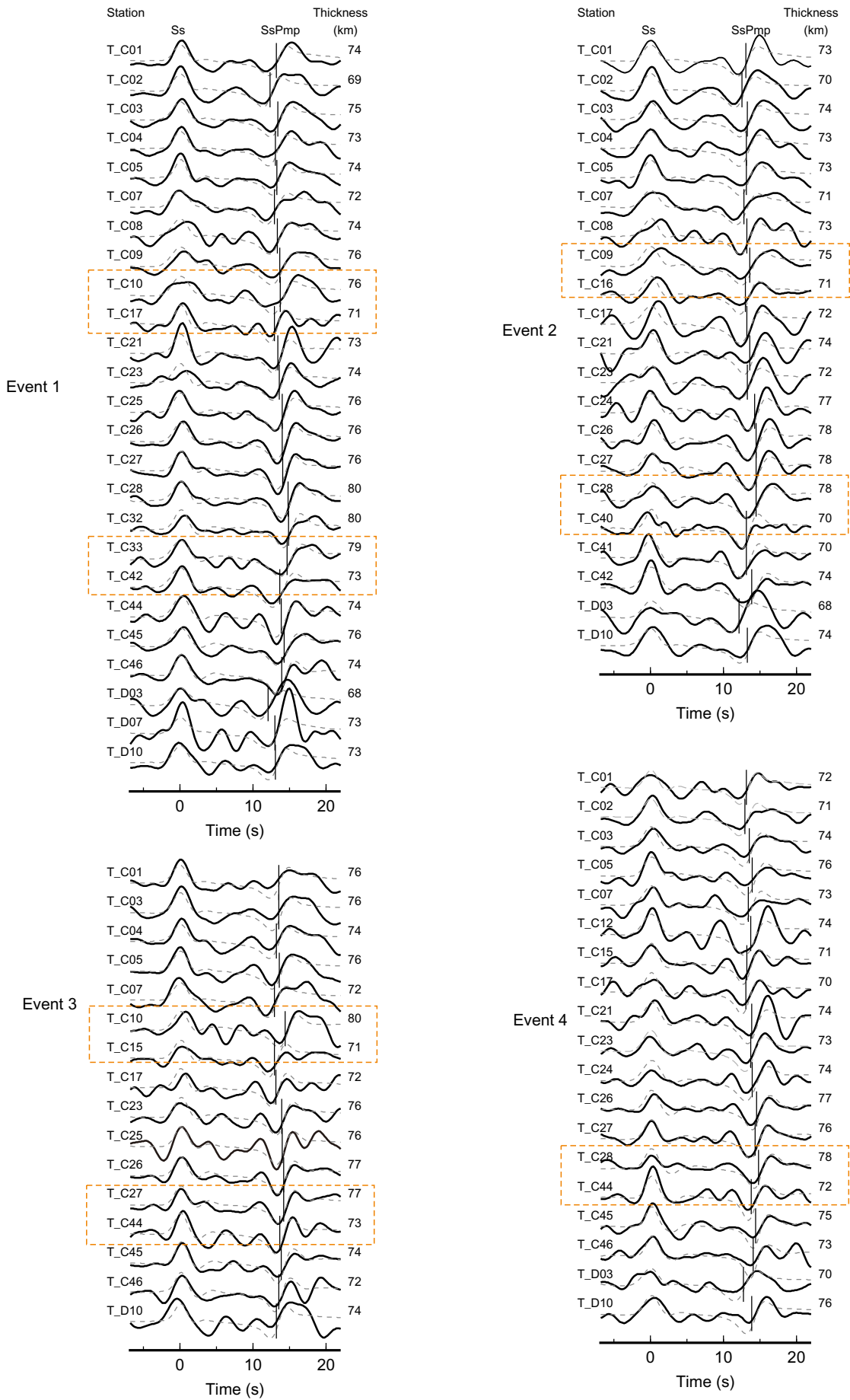


Figure S3

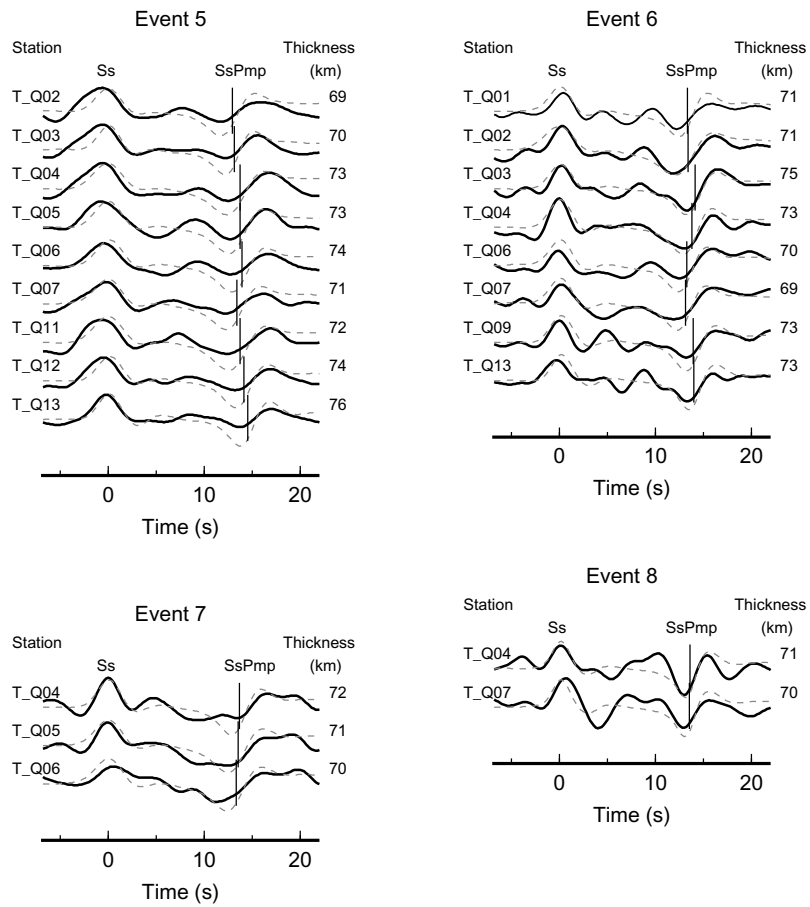


Figure S4

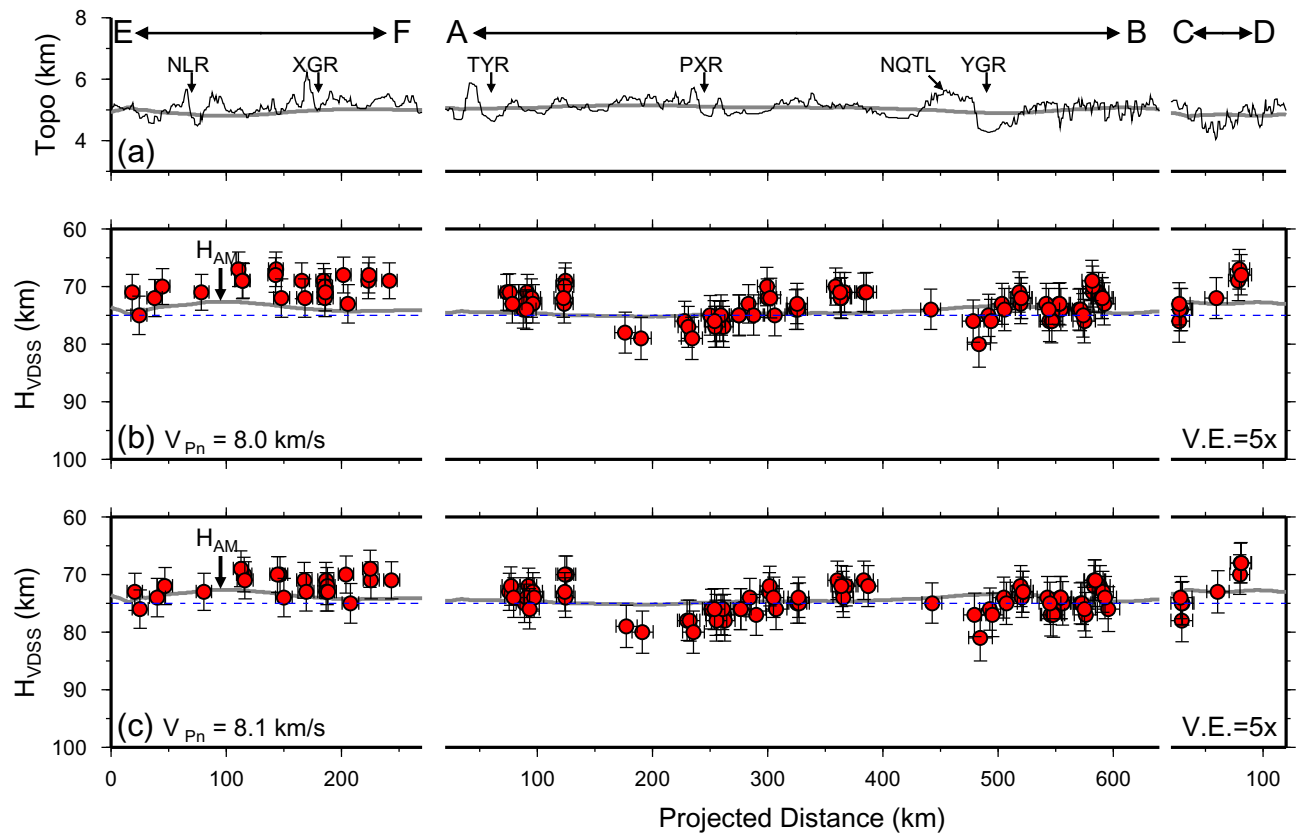


Figure S5

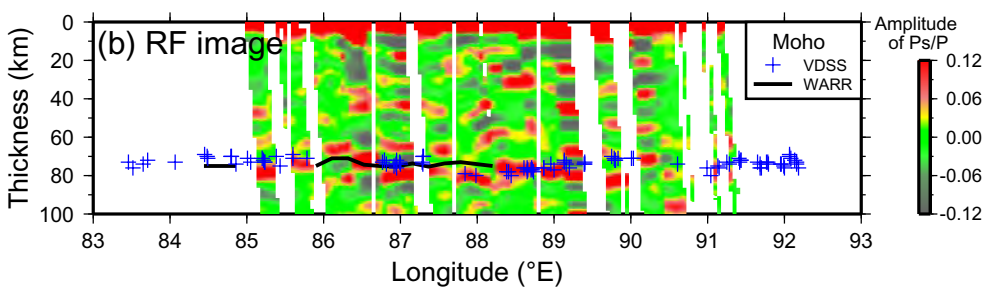
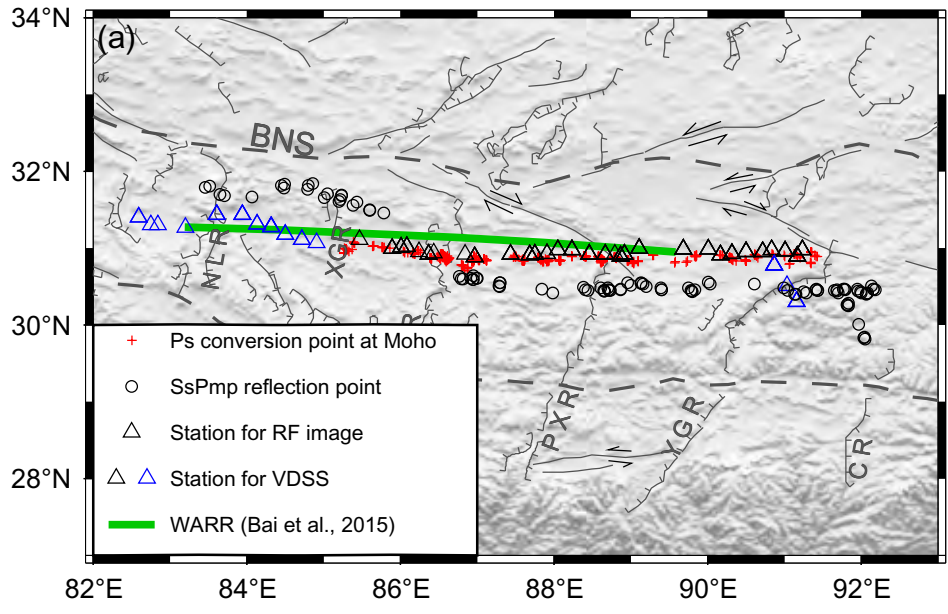
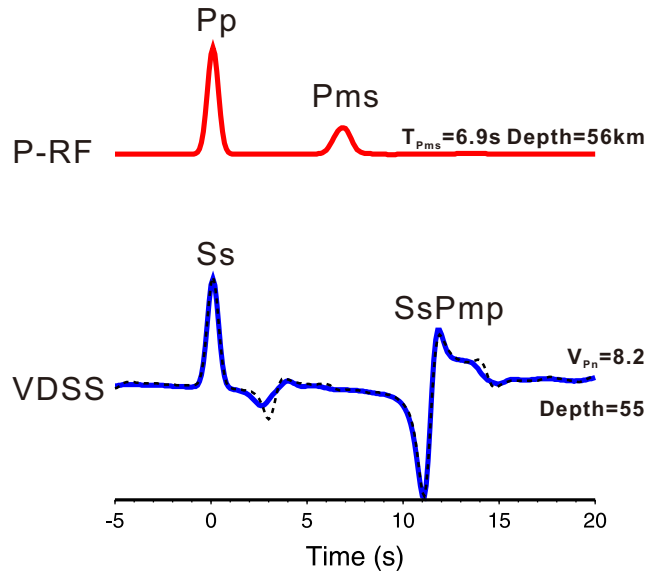
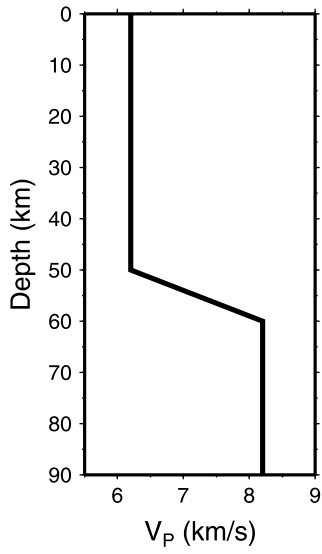
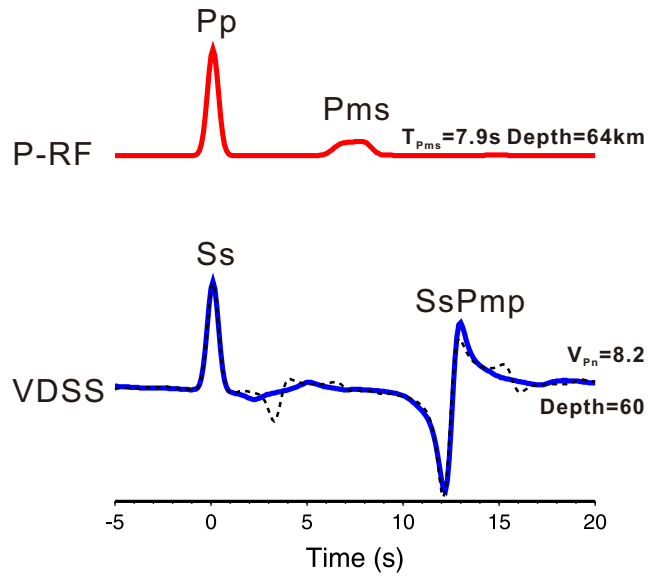
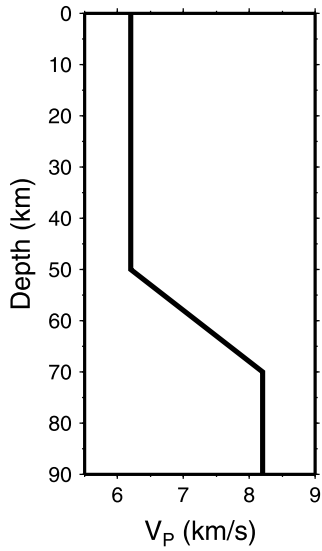


Figure S6

(a) Model 1



(b) Model 2



(c) Model3

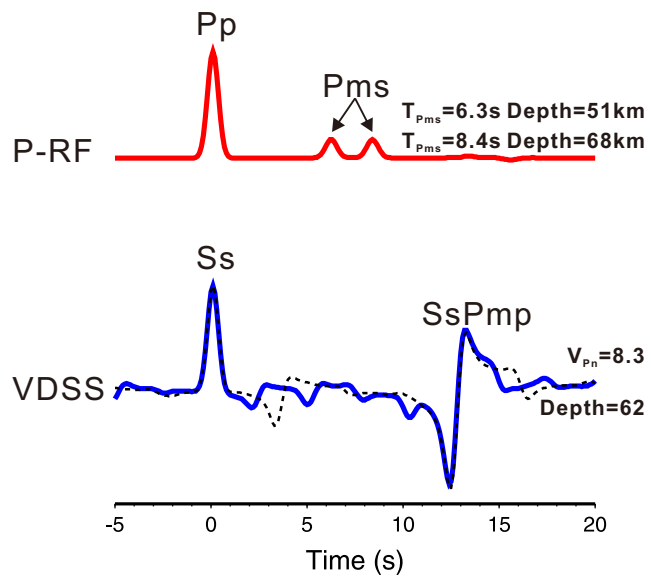
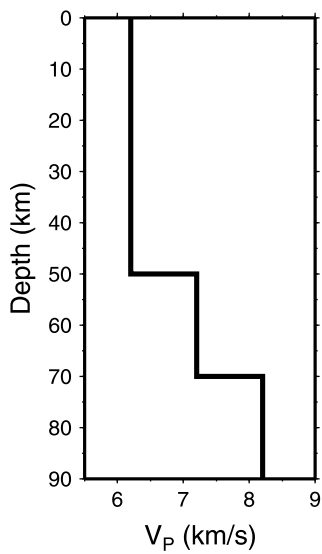


Figure S7

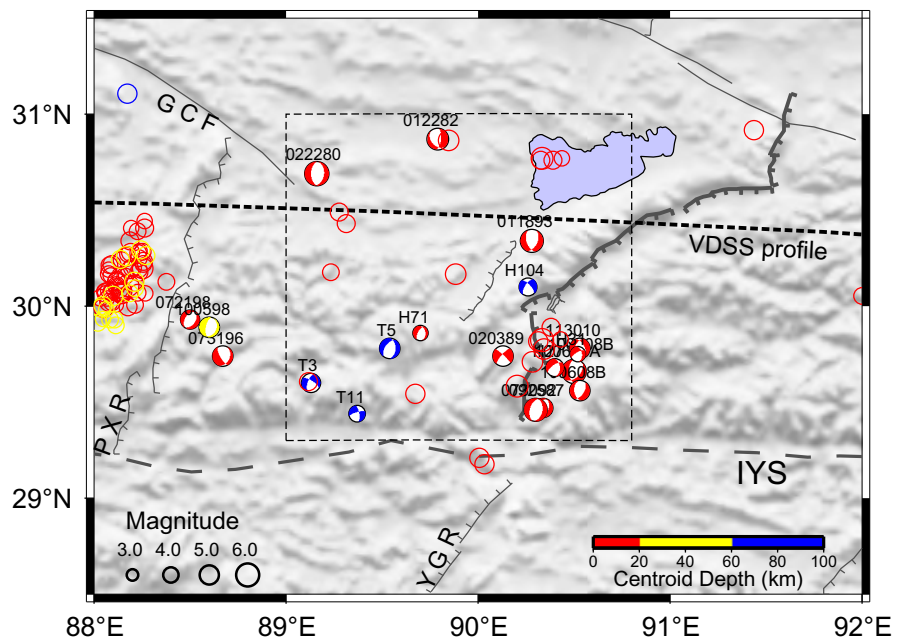


Figure S8